Pergamon

Int. J. Multiphase Flow Vol. 23, No. 5, pp. 831–844, 1997

Printed in Great Britain
PII: S0301-9322(97)00021-9
0301-9322/97 $17.00 + 0.00

STATISTICAL ANALYSIS OF VOID FLUCTUATIONS IN GAS–LIQUID FLOWS UNDER $1-g$ AND $\mu-g$ CONDITIONS USING A CAPACITANCE SENSOR

K. J. ELKOW and K. S. REZKALLAH
Department of Mechanical Engineering, University of Saskatchewan, Saskatoon, Canada S7N 5A9

(Received 21 February 1996; in revised form 28 February 1997)

Abstract—A helical wound capacitance sensor was used to obtain void fraction measurements in adiabatic two-phase water–air flow in a small diameter tube (9.53 mm, i.d.). Measurements were obtained on ground (vertical, upward) and at microgravity conditions onboard NASA's KC-135 zero-gravity aircraft. Comparisons were made between the void fraction values by matching the flow rates obtained at both $1-g$ and $\mu-g$ conditions. A statistical analysis using the Probability Density Function (PDF) was applied to the temporal void fraction signals. It was found that there was a wider fluctuation in void fraction values for the bubble and slug flow regimes at $1-g$ compared to $\mu-g$. As the two-phase mixture inertia increased, the transitional and annular flows for $1-g$ and $\mu-g$ showed similar PDF distributions.

Key Words: two-phase flow, void fraction, microgravity

1. INTRODUCTION

Improved understanding of two-phase flow characterizations can be obtained from a careful statistical analysis of the void fraction signals. Temporal fluctuations in the void fraction have been obtained in the past using signals from gamma densitometers (Jones and Zuber 1975), pressure transducers (Weisman *et al.* 1979), impedance probes (Das Pattanayak 1993; Matuszkiewicz *et al.* 1987), and non-intrusive impedance sensors (Geraets and Borst 1988; Keska *et al.* 1992). In those cases, classification of flow regime was determined from a time varying signal. In some cases the varying output alone was used, in other cases the power spectral densities, histograms and probability density functions were used to identify the flow regimes. Jones *et al.* (1981) reported measurements of void fraction fluctuations and showed PDF plots for bubble, slug, and annular flows.

2. EXPERIMENTAL SET-UP AND SIGNAL ANALYSIS

A discussion of the flight apparatus is given in Elkow (1996). The test apparatus was designed to simultaneously obtain pressure drop, heat transfer and void fraction measurements for two-phase flow. It was designed to obtain measurements on ground and also to be flown on NASA's KC-135 microgravity airplane to measure the parameters of interest under reduced gravity conditions. The major hardware components consisted of a closed liquid loop and an open gas loop. A 486/66 MHz computer was used to acquire the data and to control most of the hardware components.

The flight apparatus included a vertical test section (9.53 mm, i.d., and 1.49 m long) where pressure, void fraction, and temperatures were recorded. The void fraction sensor was a non-intrusive capacitance sensor located 620 mm, ($L/D = 65.1$) from the mixer, where air was injected into the single-phase water.

The liquid flow rate was measured using two OMEGA© turbine flow meters having a range of 0.3–9 LPM (giving $U_{SL} = 0.07$–2.1 m/s), and 0.5–15 LPM ($U_{SL} = 0.12$–3.5 m/s). For air flow measurements, two computer controlled mass flow controllers were used (0–20 SLM and

0–100 SLM (standard liters per min) ranges). A NAC Color Highspeed Video set at 1000 frames per second was used to record the two-phase flow patterns in the vertical test section. Gravity levels in the vertical test section were recorded with accelerometers provided by the Canadian Space Agency.

Details of the capacitance sensor can be found in Elkow and Rezkallah (1996). The sensor is 88 mm long. The electrodes were isolated from the flow and wound in a helix having a pitch of 29.2 mm. The active electrode length is 58.4 mm and the electrode width is 3.58 mm. A brass shield was placed over the electrodes to eliminate stray capacitance. The electronics were based on a charge/discharge principle operating at 2 MHz, as discussed by Huang *et al.* (1988). The time response of the measuring circuit has a time constant of 10 μs, corresponding to a dynamic response of 100 kHz.

Calibration of the sensor was conducted in a vertical test section 1.592 m long, using electrically triggered quick-closing valves (QCVs). Distilled and de-ionized water was used for the calibration. The superficial liquid velocities were 0.1, 0.33, 0.6, 1.0, 1.7, 2.4 and 3.3 m/s. The air flow was varied such that the widest range of void fraction could be obtained at each superficial liquid velocity setting. It was found that the sensor output was nonlinear, therefore a curve fit was applied to the data relating the void fraction trapped by the valves, the voltage output of the sensor, and the above superficial liquid velocities. Results of the calibration for the helical plate capacitor are shown in figure 1. It can be seen that most of the data fall within $\pm 10\%$ of the actual values. Using linear regression, the standard error was 0.046. There is slightly more scatter at a void fraction around 0.7 as compared with other void fraction values. This scatter is in the churn flow regime which is highly oscillatory due to the alternating "competition" between the forces of gravity pulling the fluid downward and those due to the inertia of the gas pushing the fluid upward. Measurement uncertainty of the reading for the helical wound sensor was 5% of full scale.

A signal analysis of the sensor output was conducted to ensure that there was a good signal-to-noise ratio and that aliasing was not present. For a signal frequency which is bandwidth limited to f_{max}, then a non-aliasing sample rate, f_s, would be $f_s \geqslant 2f_{max}$ Hz. This sample rate is known as the Nyquist rate (Taylor and Smith 1976). Signal analysis at 2048 Hz and 1024 Hz indicated that the majority of the frequencies for void fraction were below approximately 15 Hz. The general trend was that the amplitude decreases slightly and frequencies increased as the annular flow regime

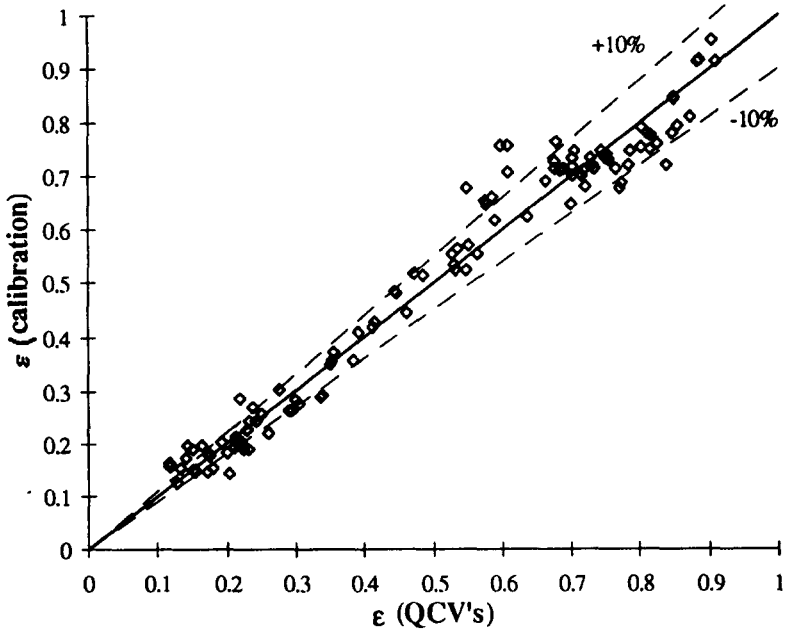

Figure 1. Calibrated void fraction for the helical plate capacitance sensor as a function of the void fraction trapped between two QCVs.

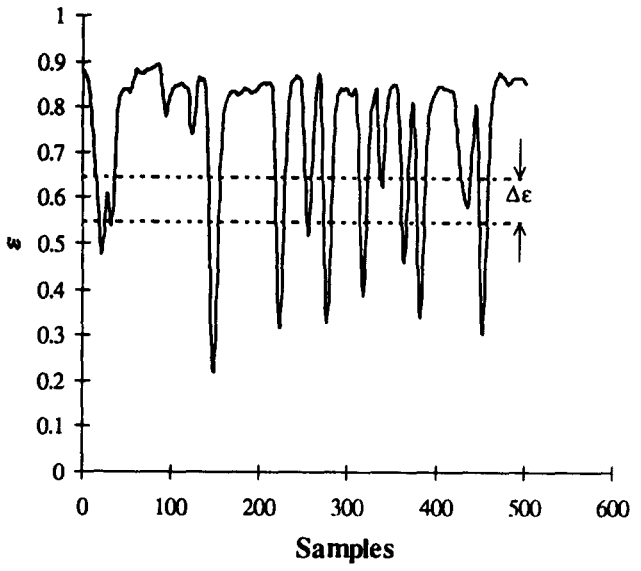

Figure 2. Void fraction signal for flight 3, parabola 9, slug flow.

was approached. Based on the Nyquist criterion a minimum sampling rate requires a rate of two times f_{max}. However, the general "rule of thumb" is to select a sampling rate 5–10 times f_{max}. Due to some limitations with the DAS, i.e. 29 channels were being used for data acquisition, a sampling rate of 70 Hz was selected. This would ensure a non-aliased signal. Furthermore, although some frequencies were slightly greater than 15 Hz, the majority were less than 10–15 Hz. Thus, 70 Hz would still provide approximately 5 times the sampling rate of those signals seen in the 10–15 Hz range.

3. PROBABILITY DENSITY FUNCTION

Discrete random variables can be plotted in a histogram which shows the frequency (on the ordinate) as a function of some measured parameter (on the abscissa for a given class width). The frequency distribution is then a collection of classes which are of equal size and cover the entire range of data without overlapping. A probability density function, (PDF) indicates the probability for a certain void fraction value to exist within a certain range, $\Delta\epsilon$. Figure 2 illustrates the method used to obtain the probability density measurement for one of the void fraction signals (Flight 3, parabola 9).

To obtain a PDF for a discrete random variable, the ordinate is divided into equal class widths, $\Delta\epsilon$. If over the total time trace the number of samples is N, and n_i is the number of occurrences within $\Delta\epsilon_i$, then the probability density function can be written as

$$p(\epsilon) = \frac{n_i}{N\Delta\epsilon_i}. \qquad [1]$$

Table 1. Data obtained from the flight and ground tests showing flow rates, gravity level, average void fraction, and flow regimes

Flight/ground parabola	U_{SL} (m/s)	U_{SG} (m/s)	Normalized gravity g_z	Average ϵ	Flow regime
94F3P22	0.86	0.09	−0.042	0.139	Bubble
94F3P13	0.24	0.19	−0.003	0.437	Slug
94F5P16	0.39	6.97	0.007	0.682	Slug–Annular
94F5P9	0.07	13.9	0.022	0.875	Annular
94G3P22	0.84	0.09	1.0	0.141	Bubble
94G3P13	0.24	0.19	1.0	0.363	Slug
94G5P16	0.40	6.92	1.0	0.721	Churn
94G5P9	0.07	13.9	1.0	0.887	Annular

4. PROBABILITY DENSITY RESULTS AND DISCUSSION

For the flight data, the average time duration consisted of approximately 400 samples (approximately 5.7 s of void fraction measurements). The selection of the "window" length depends on the stability of the g-level and both liquid and gas flow rates. For the ground data, a "window" length of 625 samples was used, which represents approximately 8.8 s of data gathering. Table 1 lists the data, in terms of the liquid and gas superficial velocities, the average void fraction and the flow regime associated with each parabola.

The data points listed in table 1 represent typical flow regimes ranging from bubble (B), slug (S), slug–annular (S–A), churn (C), to annular (A) flow. They were used to compare the PDF plots obtained with the flight and ground data. The sample coefficient of variation, cv, was used to accept or reject regions of data (Barnes 1994), and it was calculated from:

$$cv = \left(\frac{s}{\bar{x}}\right)100\%, \qquad [2]$$

where s is the sample standard deviation, and $\bar{x}$ is the sample mean. Data was retained if the sample coefficient of variation was between $\pm 7\%$ for U_{SL} and U_{SG}, and when the normalized gravity level, g_z, was within ± 0.04.

To better understand the PDF results, a description of the signal and the effect that random noise has on the signal is presented next. A PDF for single-phase water is shown in figure 3, where 5.2 V represents the average output for $\epsilon = 0$. A fluctuation around 5.2 V does not mean that the void fraction is less than zero, but rather, is due to random noise. True random noise will follow a Gaussian distribution which is defined as

$$f(x) = \frac{1}{\sigma_d\sqrt{2\pi}} e^{-(x-\mu)^2/(2\sigma_d^2)}, \quad -\infty < x < \infty, \qquad [3]$$

where the mean, μ, and the standard deviation, σ_d, determine the function $f(x)$. In addition to the PDF results shown in figure 3, a Gaussian distribution curve is also presented. It can be seen that the distribution of the noise approaches that of a Gaussian distribution and that instantaneous void fraction values below 0 or above 1.0 will, therefore, result from the noise of the system.

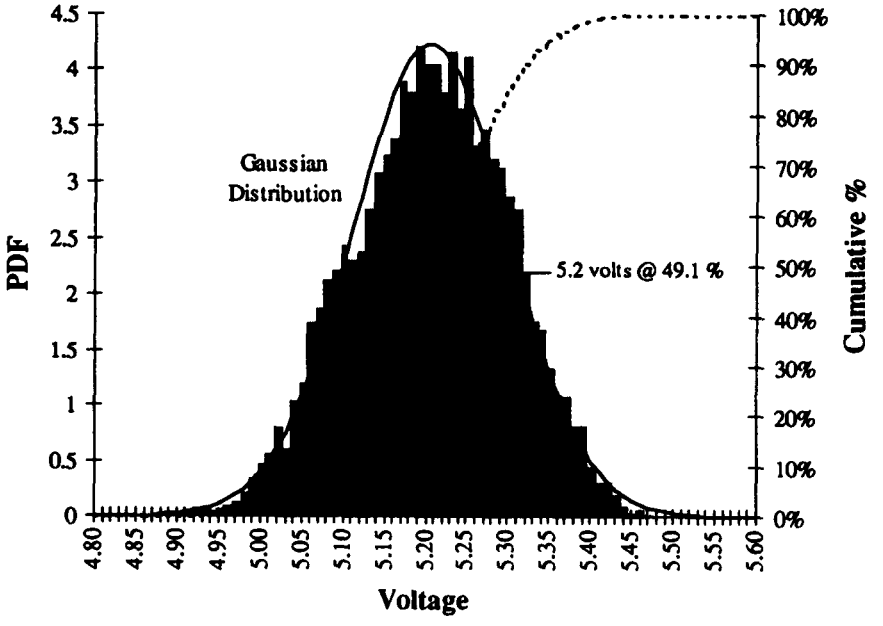

Figure 3. PDF for single-phase water.

Time trace signals, PDF plots and images of the flow regimes are shown for the parabolas listed in table 1. The PDF plots were obtained using [1] where a value of 0.01 was used for $\Delta\epsilon$. Since a flow regime can be encountered at various flow rates it is impossible to show all of the differences between the $1-g$ and $\mu-g$ data for each case. Therefore, a discussion of the differences for each flow regime will be based on the collective results from video recordings, and the analysis of the void fraction signal. The discussion will also be based on the particular flow conditions listed in table 1 and the PDF results shown.

In a comparison of the overall average void fraction values for bubble flow, given in Elkow and Rezkallah, (1997), it was found that small differences exist between the $1-g$ and $\mu-g$ cases. However, from video images and from plots of the temporal change in the void fraction values, it was found that significant differences existed. At low flow rates and at $\mu-g$ conditions, bubbles are spherical in shape, have a uniform size, and travel through the tube at regular intervals. However, at the same flow rates at $1-g$ the bubbles have a rounded leading cap and a flat tail, vary in size and flow through the tube at irregular intervals. At higher flow rates there is some added turbulence at both $1-g$ and $\mu-g$ conditions. At $\mu-g$ the bubbles are slightly distorted and somewhat elongated. There is some variation in bubble size but the majority of the bubbles

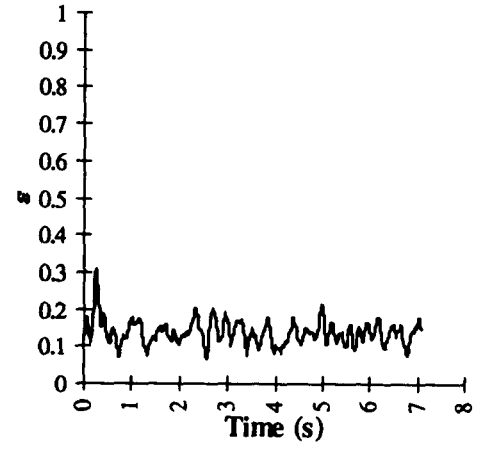

(a) Time trace for bubble flow at μ-g.

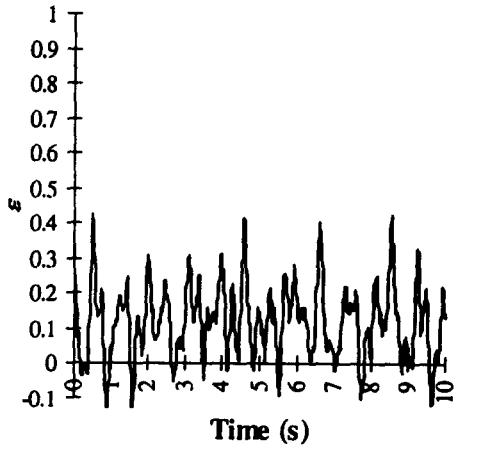

(b) Time trace for bubble flow at 1-g.

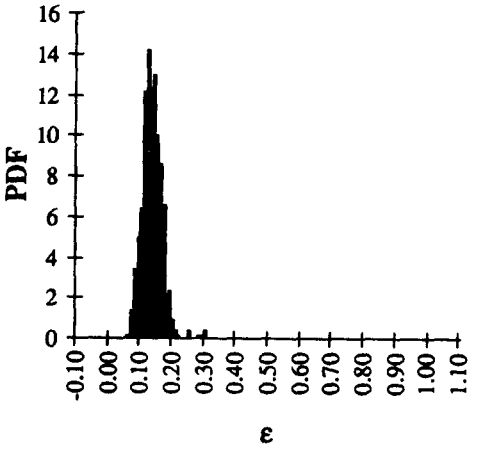

(c) PDF for bubble flow at μ-g.

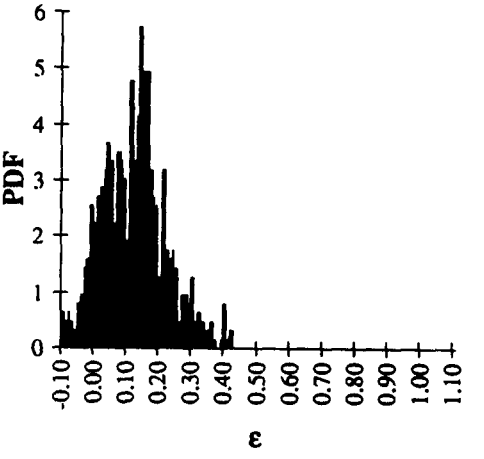

(d) PDF for bubble flow at 1-g.

Figure 4. Bubble flow regime time traces and PDF plots for data collected during Flight 3, P22, ((a) and (c)), and Ground 3, P22, ((b) and d)).

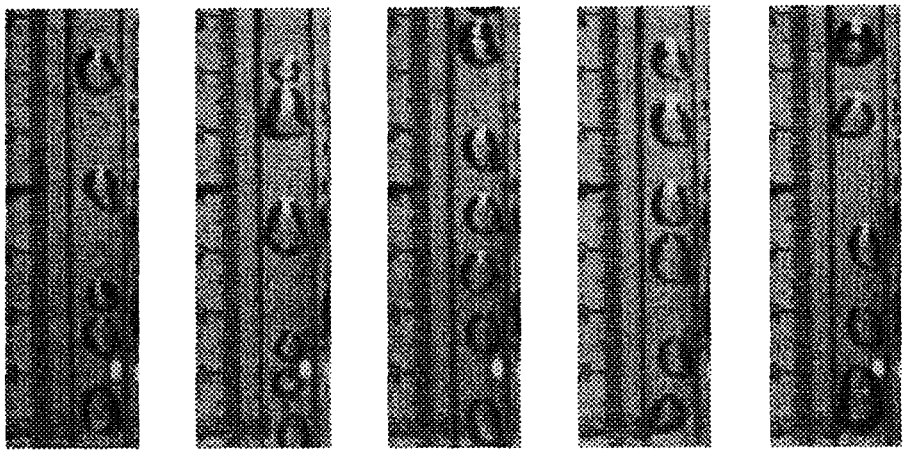

Figure 5. Sequential images for bubble flow at $\mu - g$ (Flight 3, Parabola 22).

are of similar length and still travel at regular intervals. At $1 - g$ the bubbles can be longer than those seen at $\mu - g$ and even more distorted. They tend to travel irregularly in clusters with larger bubbles leading a wide range of bubble sizes in near proximity. This could be explained perhaps in light of the "physics" of the flow, both at $1 - g$ and $\mu - g$ conditions. The predominant forces for this flow regime include buoyancy, surface tension, and turbulent stresses. At $1 - g$, forces due to gravitational acceleration tend to accelerate the bubbles and hence increase the probability of their interactions and coalescence. Thus, the void distribution varies as the bubbles agglomerate, collide, and coalesce.

Figure 4 shows the time trace and PDF plots for bubble flow at a $U_{SL} \cong 0.85$ m/s and $U_{SG} = 0.09$ m/s. The PDF plots show that the fluctuation in void fraction is much greater at $1 - g$ compared to $\mu - g$. This is clearly shown in figure 4(d) where the fluctuations of ϵ range from approximately zero to 0.40. On the other hand, at $\mu - g$ conditions, the slip velocity in bubble flow is almost zero, and the bubble movement and liquid turbulence are highly suppressed. Therefore, the bubbles remain mostly intact, moving with a uniform velocity that is more or less equal to the liquid velocity. This is also evident from the video images that were analyzed for this flow. A consecutive set of images (covering approximately 0.3 s), illustrating bubble flow can be seen in figures 5 and 6 for $\mu - g$ and $1 - g$, respectively. Although there is a limited number of frames due to space limitations, the important concepts discussed above are evident from those frames. At $\mu - g$ the bubbles are seen to be uniform in shape (approximately 1/2 tube diameter) and more equally spaced than those at $1 - g$. This uniformity at $\mu - g$ results in a narrow PDF. At $1 - g$, on the other hand, there is a wider variation in the bubble size and shape as well as the liquid

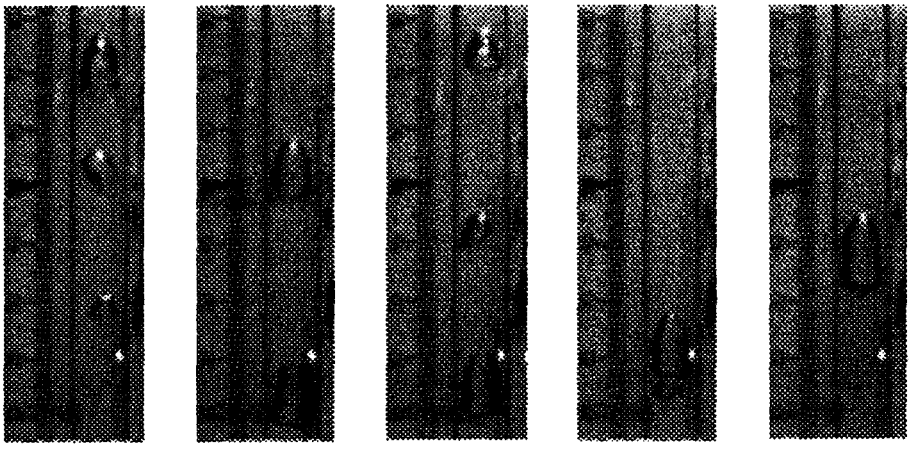

Figure 6. Sequential images for bubble flow at $1 - g$ (Ground 3, Parabola 22).

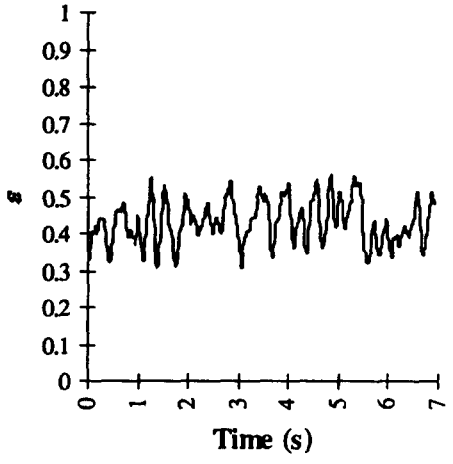

(a) Time trace for slug flow at μ-g.

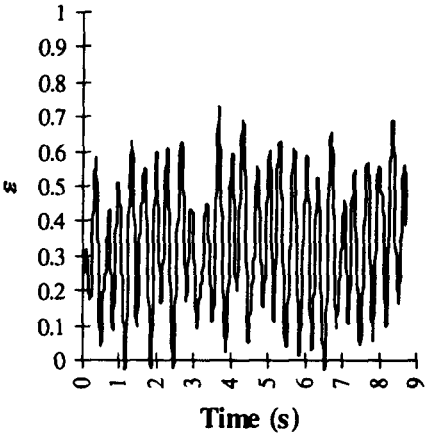

(b) Time trace for slug flow at 1-g.

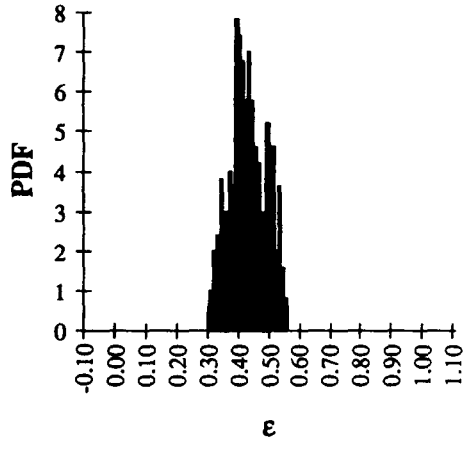

(c) PDF for slug flow at μ-g.

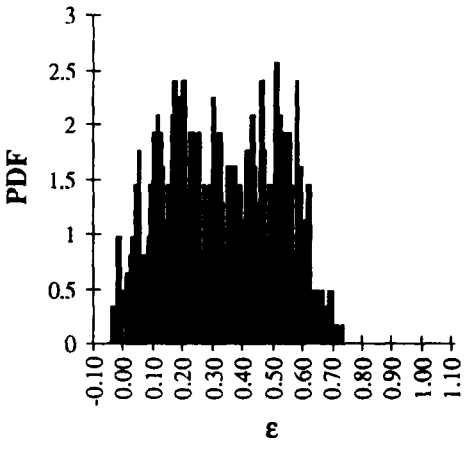

(d) PDF for slug flow at 1-g.

Figure 7. Slug flow regime time traces and PDF plots for data collected during Flight 3, P13, ((a) and (c)), and Ground 3, P13, ((b) and (d)).

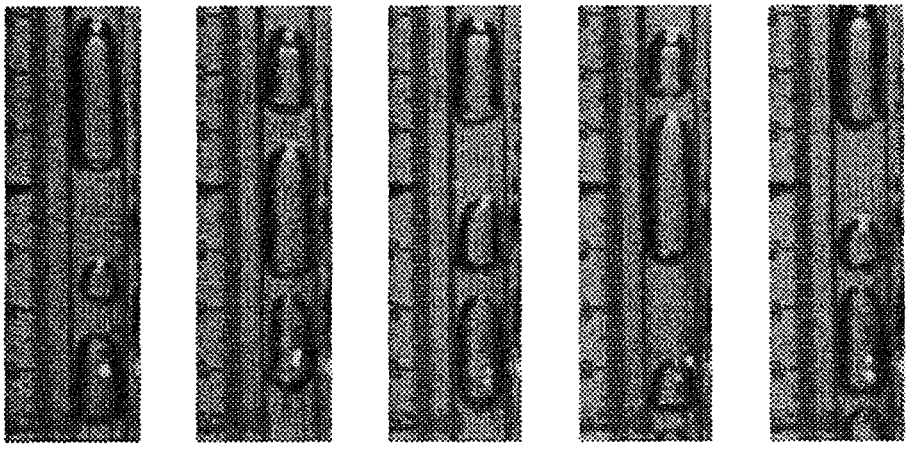

Figure 8. Sequential images for slug flow at $\mu - g$ (Flight 3, Parabola 13).

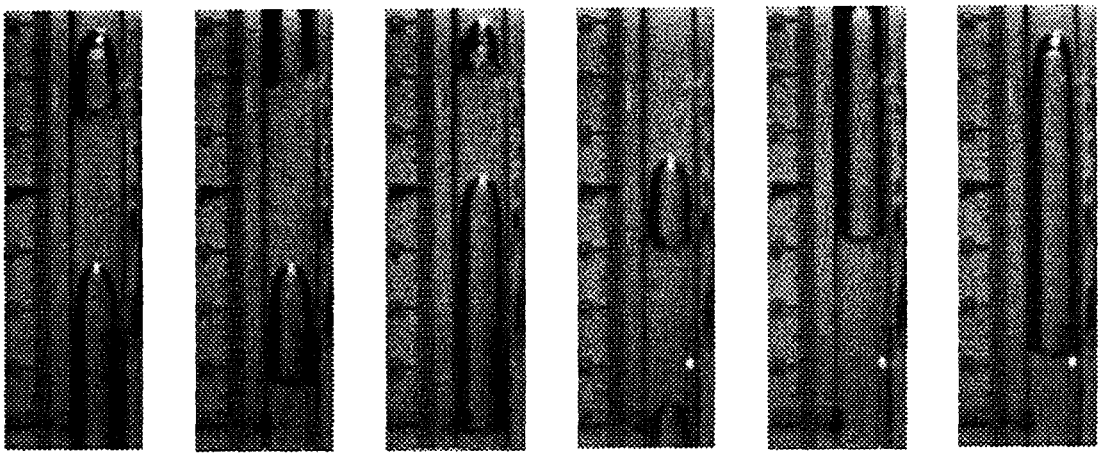

Figure 9. Sequential images for slug flow at $1-g$ (Ground 3, Parabola 13).

separating them, causing a greater fluctuation in the PDF. Bubble diameters vary from a few millimeters to approximately 1 tube diameter. Liquid separating the bubbles range from a few bubble diameters to spacing of about 6–7 tube diameters. In terms of the PDF distribution, as shown in figure 4(c), the spectrum of variation of ϵ at $\mu-g$ is limited in the range of $0.08 < \epsilon < 0.20$. Within this void fraction range, it can be seen that the mean value that occurs at $\mu-g$ has a much higher probability of occurrence (approximately 2 times that of the $1-g$ counterparts).

These are important findings that can perhaps explain the lower heat transfer coefficients associated with bubble flow at $\mu-g$ conditions. Rite (1995) reported that in the range of $0.10 < \epsilon < 0.18$, the heat transfer coefficients for bubble flow at $1-g$ were 3–12% higher than those measured at $\mu-g$. The higher heat transfer rates at $1-g$ are attributed to the larger bubble fluctuations, and the higher mixture turbulence. Hence better heat transfer rates are achieved with higher mixing of the flow.

Typical time traces and PDF plots for slug flow are presented in figure 7 with images of the flow at $\mu-g$ and $1-g$ conditions shown in figures 8 and 9, respectively. The flow conditions are at relatively low liquid and gas flow rates ($U_{SL} = 0.24$ m/s and $U_{SG} = 0.19$ m/s). The elapsed time covered in figures 8 and 9 was approximately 0.5 s. A comparison of the average void fraction values for slug flow at $1-g$ and $\mu-g$ show that the overall average void fraction values at $\mu-g$ conditions were approximately 10% higher (see Elkow and Rezkallah 1997).

The signal output for slug flow is therefore characterized by high and low ϵ values, depending on which phase is flowing in the conduit at that time. This is obvious from the signal trace shown in figure 7(a) and (b). Due to buoyancy at $1-g$, coalescence occurs rapidly under those conditions, and the time trace shows large fluctuations around a mean value. The coalescence observed at such low flow rates is primarily due to Taylor bubbles coming into contact with each other rather than coalescence due to small bubbles merging into them (conditions that are very common at higher gas content at $1-g$). Since buoyancy is negligible under $\mu-g$ conditions, the Taylor bubbles are seen to move with equal velocity resulting in little to no interaction, hence uniform bubble length and considerably smaller fluctuation in the void fraction is observed (figure 7(a)). Hence, the spread of the void fraction signal is far more significant under $1-g$ compared to $\mu-g$; see figure 7(b).

The lesser fluctuations at $\mu-g$ are also reflected in the PDF plots; figure 7(c) and (d). The PDF from the $\mu-g$ data for slug flow covers a much narrower spectrum when compared to $1-g$, indicating more uniform bubbles with less variation in the void fraction in the liquid slug. Under $\mu-g$ conditions ϵ changes only between approximately 0.3–0.55, while at $1-g$ the range is between almost zero up to 0.75.

Ideally, slug flow should show two peaks on a PDF histogram; one associated with the liquid slug, and the other with the Taylor bubble. With the ground data, the development of the two peaks can be seen in figure 7(d) with one at approximately $\epsilon = 0.20$ and the other at approximately $\epsilon = 0.60$. The distinctiveness of the peaks depends mainly on the geometry of the sensor, and to

a lesser extent on the flow itself; i.e. the length of the Taylor bubble, and the length of the liquid slug. Since the sensor measures a volumetric void fraction, the signal is "filtered" for certain bubble sizes. As a result of the sensor length, distinct peaks at a low and high void fraction are not seen. If either the bubble or the liquid slug are shorter than the sensor, the sensor does not see the two extreme void fraction values but an "overall" average reading between the two. This was the case at $\mu - g$ conditions where only a single peak was registered. This is primarily due to the short liquid slugs separating the bubbles. In general, as seen in the recorded images, at no time was the sensor filled with liquid only. Thus, an average void fraction representing the bubble and slug was always read. Observations of the numerous video images at $\mu - g$ indicate that this type of flow is quite predictable in that the slugs were essentially stable and of equal length (seen in figure 8). This is also evident in the PDF plot, with a high probability at the average void fraction value and very little variation about the average.

Further discussion and interpretation of the PDF results can be made based on the flow images shown in figures 8 and 9. Taylor bubble like flows at $\mu - g$ are more uniform in length. The Taylor bubbles at $\mu - g$ vary from only 1–3 tube diameters, whereas at $1 - g$ the Taylor bubble for the

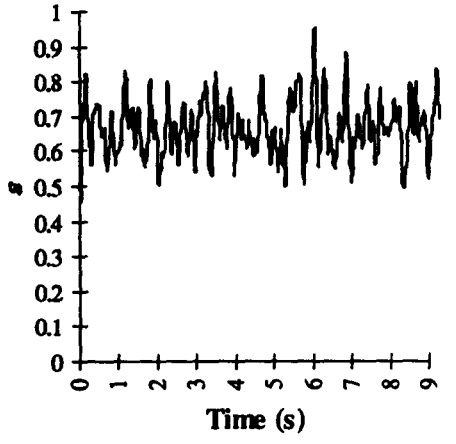

(a) Time trace for slug-annular flow at μ-g.

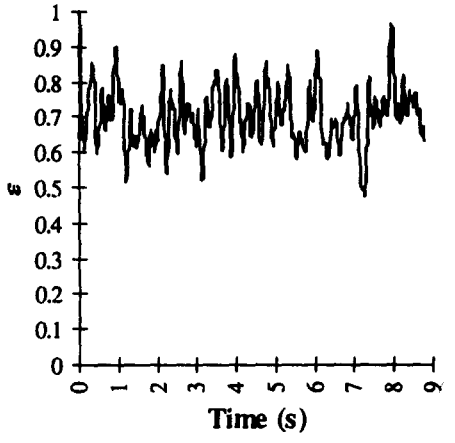

(b) Time trace for churn flow at 1-g.

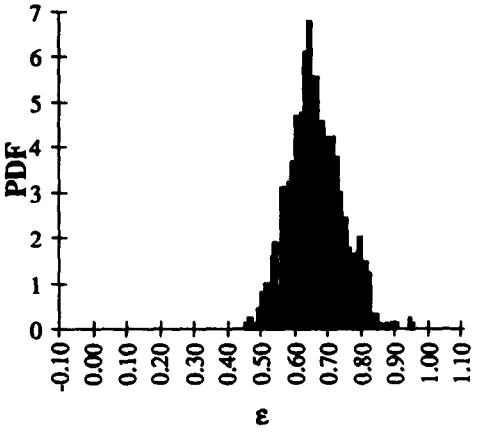

(c) PDF for slug-annular flow at μ-g.

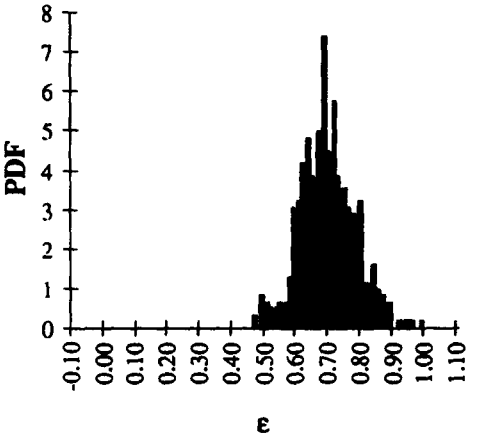

(d) PDF for churn flow at 1-g.

Figure 10. Slug–annular and churn flow regime time traces and PDF plots for data collected during Flight 5, P16, ((a) and (c)), and Ground 5, P16, ((b) and (d)).

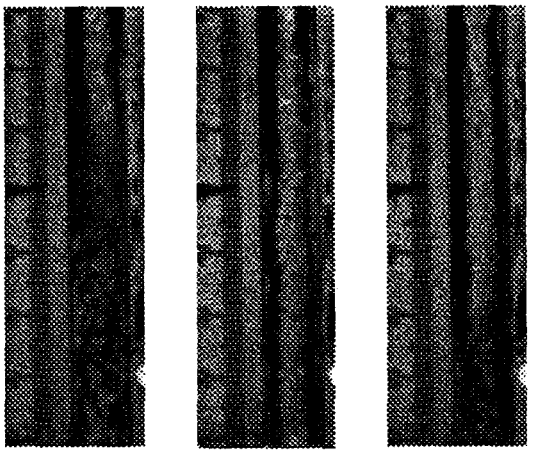

Figure 11. Images of slug–annular flow at $\mu - g$ (Flight 5, Parabola 16).

same flow rates ranges from 1–6 tube diameters. Further evidence of the effects of buoyancy can be seen in the flatter trailing end of the Taylor bubble at $1 - g$ (figure 9), whereas the trailing end of the Taylor bubble at $\mu - g$ (shown in figure 8) where buoyancy is negligible, is seen to be more rounded. Buoyancy causes a relative velocity difference between the liquid and gas phases. With the gas phase having the higher velocity, a low pressure region at the tail of the Taylor bubble would occur. From the video recordings in this region, it has been observed that coalescence is enhanced when another Taylor bubble approaches this low pressure region. However, at $\mu - g$ there is essentially no slip, thus a low pressure region at the tail of a Taylor bubble does not exist. It has been observed from these video recordings that Taylor bubbles within close proximity to each other rarely coalesce at $\mu - g$.

Temperature measurements in slug flow, as reported by Rite (1995), indicate that the heat transfer coefficients at $1 - g$ can be 30–40% higher than their counterparts at $\mu - g$ (corresponding to a void fraction from approximately 0.3 to 0.65). As the void fraction increased, the difference in the heat transfer coefficients was minimum. This could be perhaps explained in terms of the results shown in figure 7(c) and (d). As already stated, the PDF scatter at $1 - g$ is larger than that at $\mu - g$, indicating that a wider range of bubbles are present in the $1 - g$ flow. This could result in enhanced mixing in the slug region of the flow; thereby resulting in a higher heat transfer coefficient.

The next series of plots, shown in figure 10, are those for the transitional slug-to annular flow (churn flow regime at $1 - g$). Images of the flow at $U_{SL} \cong 0.39$ m/s and $U_{SG} \cong 6.97$ m/s can be seen in figures 11 and 12. This transition is the result of increasing the gas flow rate to the point where

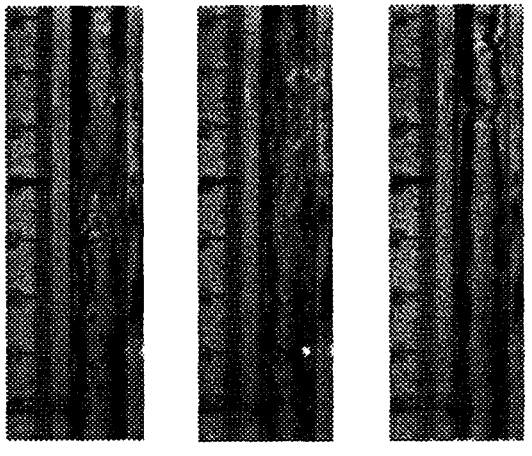

Figure 12. Images of churn flow at $1 - g$ (Ground 5, Parabola 16).

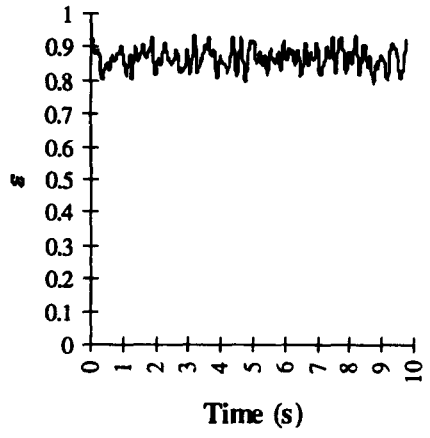

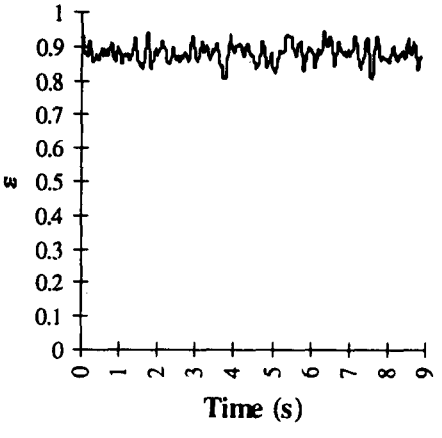

(a) Time trace for annular flow at μ-g. **(b) Time trace for annular flow at 1-g.**

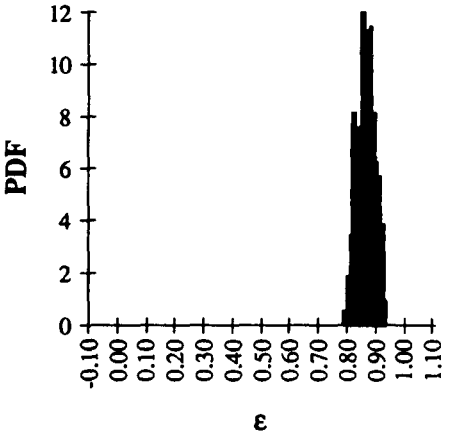

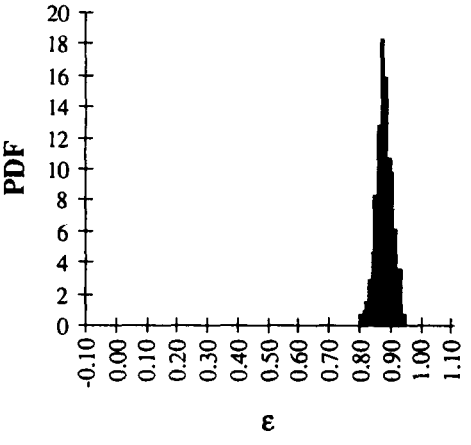

(c) PDF for annular flow at μ-g. **(d) PDF for annular flow at 1-g.**

Figure 13. Annular flow regime time traces and PDF plots for data collected during Flight 5, P9, ((a) and (c)), and Ground 5, P9, ((b) and (d)).

Figure 14. Images of annular flow at $\mu - g$ (Flight 5, Parabola 9).

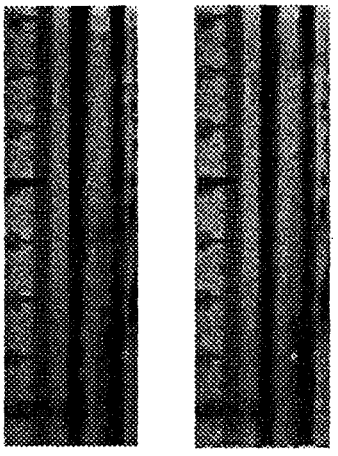

Figure 15. Images of annular flow at $1-g$ (Ground 5, Parabola 9).

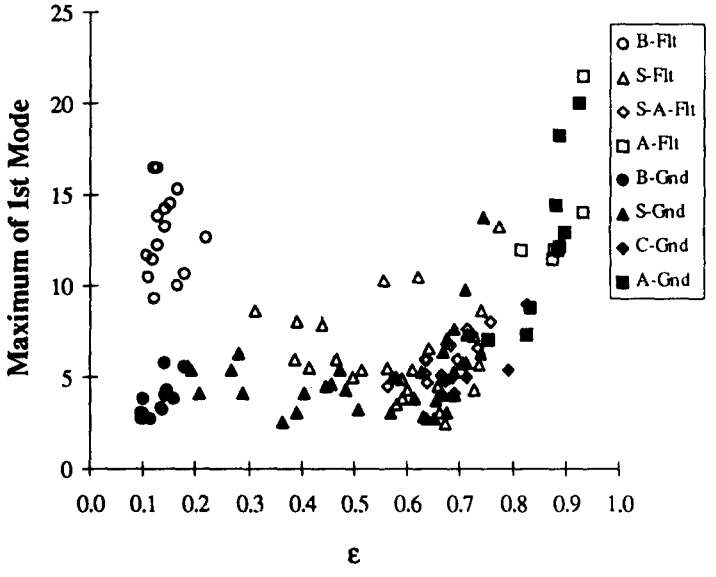

Figure 16. Maximum value of the first mode as a function of void fraction for the $1-g$ and $\mu-g$ data.

the gas phase becomes a continuous phase (annular flow) with little or no liquid bridging at the center. At $1-g$, churn flow is observed in this region. Due to the pull of gravity on the liquid phase, churn flow is characterized by large oscillations and continuous liquid bridging. The average void fraction in both cases was found to be similar as shown in Elkow and Rezkallah, (1997). It can be also seen from figure 10 that the time trace and the PDF plots are very similar. This is mainly due to the fact that inertia forces are starting to dominate, and hence gravity plays a much lesser role. The interface between the liquid and gas becomes wavy as the bubble length grows. As the waves are sheared by the incoming gas, liquid is entrained into the gas core and a "frothy" mixture is formed in the liquid regions. The similarities in this flow regime can be seen in the flow images given in figures 11 and 12 for $\mu-g$ and $1-g$ flows, respectively.

The heat transfer results showed that the slug-annular and annular heat transfer coefficients approached similar values for both $1-g$ and $\mu-g$ data (Rite 1995). Some of the data showed that the $\mu-g$ heat transfer coefficients were slightly higher in the slug–annular regime (approximately 10% higher). However, this was approaching the measurement uncertainty of the heat transfer data. Although the PDF plots and void fraction signals appear similar, the heat transfer for this regime would be determined by the froth present in the slug–annular flow at $\mu-g$ and the degree of churning at $1-g$ (since both are becoming inertia dominant flows).

Finally, the annular flow results are shown in figure 13 for $U_{SL} = 0.07$ m/s and $U_{SG} = 13.9$ m/s. Corresponding images of the flow are shown in figures 14 and 15 for $\mu - g$ and $1 - g$, respectively. In that flow, inertia forces are very significant and dominate by far all other body forces acting on the flow (e.g. surface tension force). Thus, it is expected that the effect of gravity is negligible in this regime. In both cases, a liquid film is retained at the tube wall, with the gas phase occupying the center of the tube. Thus, no great difference should be expected with respect to the volumetric void fraction results. This is seen in figure 13 with similar time traces, width and maximum values of the PDF distribution. In general the average void fraction values for this flow are also similar (see table 1).

In addition to examining the individual PDF plots for the flight and ground data, figure 16 is used to show a complete presentation of the void fraction since the same flow regime can occur at various flow rates and void fraction. Figure 16 is a plot of the maximum value of the first mode of the PDF as a function of void fraction for both sets of data. A mode of a PDF occurs whenever there is a local maximum in $f(\epsilon)$. This means that a maximum value will occur in $f(\epsilon)$ at some void fraction, ϵ_1, and all values near ϵ_1 will be less than $f(\epsilon_1)$. More than one mode may exist, corresponding to each local maximum. The first mode is considered to be the greatest local maximum, the second mode is the next greatest local maximum, etc. Figure 16 shows only the first mode as a function of the measured void fraction. The area under a PDF is equal to one. Therefore, for bubble and annular flow regimes (where only one peak in the PDF occurs), a high value for the first mode will imply a narrower fluctuation in void fraction. Conversely, a lower value for the first mode will imply a wider void fraction fluctuation.

For the flight data, it can be seen from figure 16 that the first mode of the PDF is higher than that for the ground data (up to a void fraction of approximately 0.70). At a void fraction of 0.70 (which would represent the region where forces due to inertia begin to dominate), the two data sets merge into each other. For void fraction values greater than 0.70, the $1 - g$ and the $\mu - g$ results are almost identical.

5. CONCLUSIONS

Using a helical wound capacitance void fraction sensor, volumetric void fraction measurements were obtained for adiabatic two-phase, water–air data at $1 - g$ and $\mu - g$. The data was collected for flow in a 9.53 mm, i.d. tube over a wide range of liquid and gas flow rates, covering a range of void fraction from approximately 0.10–0.90. The test section was oriented vertically on ground and with respect to the aircraft floor. Comparisons of time traces and PDF histograms for the void fraction signals at $1 - g$ and $\mu - g$ were made. In summary, the following conclusions could be made:

(1) The PDF histograms for bubble flow showed a much greater fluctuation in void fraction at $1 - g$ (in the range, $0 < \epsilon < 0.4$); whereas the void fraction at $\mu - g$ showed a narrower range, $(0.1 < \epsilon < 0.2)$. At $\mu - g$, the slip velocity between the phases is essentially zero, resulting in suppressed turbulence and lesser interactions between bubbles.

(2) The PDF histograms for slug flow also indicated a greater fluctuation in void fraction for the data collected at $1 - g$. Fluctuations were in the range, $0 < \epsilon < 0.75$, for $1 - g$, and restricted only to the range, $0.3 < \epsilon < 0.55$ for the $\mu - g$ data. In addition, the overall average of the void fraction values in this regime was approximately 10% higher in $\mu - g$.

(3) As with the average void fraction values for slug-annular and churn flow, the PDF plots were also found to be similar. Void fluctuations from approximately 0.5–0.9 were observed for both $1 - g$ and $\mu - g$ flows. This could be attributed to the fact that inertia is becoming dominant; thus reducing any differences that were previously seen.

(4) The PDF histograms for annular flow were found to be similar for both $1 - g$ and $\mu - g$ flows. A very narrow fluctuation from approximately $0.8 < \epsilon < 0.9$ was observed. This is expected since the flow in this regime is highly inertia dominated.

(5) Analysis of the first mode of the PDF plots shows that the slug-to-annular transitional flow occurs at a void fraction of approximately 0.7. Beyond this region, differences between $1 - g$ and $\mu - g$ data are extremely insignificant.

REFERENCES

Barnes, J. W. (1994) *Statistical Analysis for Engineers and Scientists a Computer-based Approach*. McGraw-Hill, New York.

Das R. K. and Pattanayak, S. (1993) Electrical impedance method for flow regime identification in vertical upward gas–liquid two-phase flow. *Meas. Sci. Technol.* **4,** 1457–1463.

Elkow, K. J. (1996) Void fraction measurement and analysis at normal gravity and microgravity conditions. M.Sc. thesis, Saskatoon, University of Saskatchewan.

Elkow, K. J. and Rezkallah, K. S. (1996) Void fraction measurements in gas–liquid flows using capacitance sensors. *Meas. Sci. Technol.* **7,** 1153–1163.

Elkow, K. J. and Rezkallah, K. S. (1997) Void fraction measurements in gas–liquid flows under $1-g$ and $\mu-g$ conditions using capacitance sensors. *Int. J. Multiphase Flow* (to appear).

Geraets, J. J. M. and Borst, J. C. (1988). A capacitance sensor for two-phase void fraction measurement and flow pattern identification. *Int. J. Multiphase Flow* **14,** 305–320.

Huang, S. M., Stott, A. L., Green, R. G. and Beck, M. S. (1988) Electronic transducers for industrial measurement of low value capacitances. *J. Phys. E: Sci. Instrum.* **21,** 242–250.

Jones, O. C. Jr, Abuaf, N., Zimmer, A. and Feierabend, T. (1981) Void fluctuation dynamics and measurement techniques. In *Two-phase Flow Dynamics*, ed. A. E. Bergles and S. Ishigai, pp. 145–163. McGraw-Hill, Washington.

Jones, O. C. Jr and Zuber, N. (1975) The interrelation between void fraction fluctuations and flow patterns in two-phase flow. *Int. J. Multiphase Flow* **2,** 273–306.

Keska, J. K., Fernando, R. D. and Hamer, M. T. (1992) Experimental study of temporal fluctuation of physical parameters in an air–water two-phase flow in a small horizontal square channel based on the *in situ* measurement of concentration with a computer based system. *ANS Proceedings, National Heat Transfer Conference*, Vol. 6, 9–12 August, San Diego, CA.

Matuszkiewicz, A., Flamand, J. C. and Boure, J. A. (1987) The bubble–slug flow pattern transition and instabilities of void fraction waves. *Int. J. Multiphase Flow* **13,** 199–217.

Rite, R. W. (1995) Heat transfer in gas–liquid flows through a vertical circular tube under microgravity conditions. Ph.D. thesis, Saskatoon, University of Saskatchewan.

Taylor, F. and Smith, S. L. (1976) *Digital Signal Processing in Fortran*. Lexington Books, Lexington, MA.

Weisman, J., Duncan, D., Gibson, J. and Crawford, T. (1979) Effects of fluid properties and pipe diameter on two-phase flow patterns in horizontal lines. *Int. J. Multiphase Flow* **5,** 437–462.